Solar Physics (2023) 298:117
https://doi.org/10.1007/s11207-023-02210-w

RESEARCH

Plasma Heating in an Erupting Prominence Detected from Microwave Observations with the Siberian Radioheliograph

A.M. Uralov[1] · V.V. Grechnev[1] · S.V. Lesovoi[1] · M.V. Globa[1]

Received: 9 June 2023 / Accepted: 20 September 2023

Abstract
A major eruptive flare occurred on 12 January 2022 in the northeast not far behind the solar limb (N32 E116). The eruption produced a fast coronal mass ejection (CME). The rising ejecta was observed by the telescopes in the extreme ultraviolet and by the multi-frequency *Siberian Radioheliograph* (SRH) in the 5.8 – 11.8 GHz range. We show how the slope of the decrease in the brightness temperature of the rising ejecta, measured from the microwave SRH images, is related to the heat inflow or outflow in its body during rapid expansion with high acceleration and under the assumption that the plasma ionization state changes insignificantly within the measurement interval. We found that the low-temperature plasma component in the erupting prominence underwent heating. Most likely, this was due to the predominance of ohmic heating because i) the polytropic index of expanding plasma expected in this case was closest to the experimentally measured one, and ii) the ohmic dissipation due to electron-proton collisions loses its efficiency during expansion much slower than the other mechanisms of heating or cooling.

Keywords Coronal mass ejections · Heating · Prominences · Radio emission

1. Introduction

The presence of heating sources for the plasma of the solar atmosphere is beyond doubt. The approximation of a static atmosphere implies a thermal balance which means that the heat inflow into a selected element of space is equal to its outflow to the outside. In a stationary solar wind, there must be an inflow of heat; otherwise, it could not be formed. However, the solar wind flows in open magnetic structures. In non-stationary phenomena, such as

✉ V.V. Grechnev
grechnev@iszf.irk.ru

A.M. Uralov
uralov@iszf.irk.ru

S.V. Lesovoi
svlesovoi@gmail.com

M.V. Globa
globa@iszf.irk.ru

[1] Institute of Solar-Terrestrial Physics SB RAS, Lermontov St. 126A, Irkutsk 664033, Russia

Published online: 06 October 2023

ejections of solar plasma confined in closed magnetic structures, the assumption of a thermal balance in a moving plasma element may be violated. The question arises as to the direction of this violation. In other words, the inflow of heat or its outflow prevails. If they are equal or simply absent, the ejected plasma expands adiabatically.

Observations of eruptive filaments (prominences) do not answer to this question unambiguously. For example, eruptions of filaments from active regions are often accompanied by considerable rapid heating to coronal or higher temperatures of part of the plasma that they contain. This can be seen in the extreme ultraviolet (EUV) as a change in the visibility of the prominence from absorption to emission during the early periods of the eruption (e.g. Filippov and Koutchmy, 2002; Lee et al., 2017). Moreover, such a transformation of prominence visibility is sometimes observed even before the launch of a fast eruption. There are indications (Kucera and Landi, 2008) of heating of slowly erupting prominences whose plasma does not reach coronal temperatures. In general, it is not clear if heating continues after the eruption begins, while such heating has been confirmed in a few case studies (Akmal et al., 2001; Glesener et al., 2013; Grechnev et al., 2016, 2019). On the other hand, eruptions of quiescent filaments far from active regions and plages show no signs of prelaunch heating of low-temperature filament plasma at all. It seems that the expansion of such filaments is accompanied only by their adiabatic cooling. What happens to prominences in terms of heating in a wider set of eruptions remains unclear.

The answer can be found in measuring the rate of change in the temperature of the expanding plasma in an ejecta. Microwave observations of solar filaments have long been a direct method for estimating their plasma temperature and emission measure. The main body of most quiescent filaments and prominences is a low-temperature plasma located above the chromosphere-corona transition region. Screening the quiet-Sun's emission in the centimetric and a part of the millimetric range, the filaments look like depressions, whose core coincides with the depressions visible in the Hα line (e.g., Rao and Kundu, 1977; Lantos and Raoult, 1980). In this case, solar filaments are optically thick and, with sufficient angular resolution, their brightness temperatures are close to the kinetic temperatures of cold hydrogen plasma.

The brightness temperatures of filaments located outside active regions range from about 4000 K to about 10000 K both before and during their relatively slow eruptions (e.g., Zandanov and Lesovoi, 1999; Grechnev et al., 2006). At wavelengths shorter than about 3 mm, the optical thickness of quiescent filaments becomes less than unity, and the depression effect gradually disappears (e.g., Heinzel et al., 2022). The fact that solar filaments absorb radio emission from the quiet Sun, even in the millimeter range, indicates that the degree of ionization of hydrogen plasma at temperatures from about 4000 K and a number density of plasma particles of the order of $10^{10}-10^{12}$ cm^{-3} are high enough to provide the necessary for absorption opacity.

In a real situation, the ionization state of static plasma that strongly departs from local thermodynamic equilibrium (LTE) depends significantly on the specific values of temperature, density, and fluxes of photoionizing optical and ultraviolet radiation. In turn, these quantities depend on the shape of the prominence and its height above the photosphere. All the listed parameters are ambiguous, and it is impossible to specify any characteristic value of the degree of ionization.

To an even greater extent, such ambiguity is inherent in dynamic plasma during an impulsive eruption of a filament (prominence) from an active region when, among other things, at the beginning of the eruption, a part of the initially cold hydrogen plasma is considerably heated (e.g., Grechnev et al., 2019). Nevertheless, the very dynamism of the expanding plasma may suggest the source of its heating.

In the present study, we use the radio method and the fact of the rapid expansion of an eruptive prominence to figure out the heating mechanism for the main part of its plasma. The experimental basis of our study is microwave images of an eruptive prominence obtained by the *Siberian Radioheliograph* (SRH: Altyntsev et al., 2020) in test observations. The distance dependence of the brightness temperature of a piece of an erupting prominence is measured. The experimentally obtained dependence is then compared with that calculated under the assumption that the expansion of the prominence plasma is governed by the polytropic pattern. That is, the product pV^{α} of the pressure $[p]$ and volume $[V]$ of the plasma piece is a constant, and α is the polytropic index. This method makes it possible to estimate from radio data the amount of heat released in the plasma during eruption. In the case of adiabatic expansion, the polytropic index would be equal to the adiabatic index $\gamma = 5/3$.

2. The 12 January 2022 Eruptive Event

2.1. Brief Description of the Event and Its Observations

We consider the eruptive event that occurred on 12 January 2022, starting at about 04:25 over the solar limb in the northeast. The eruption resulted in a fast coronal mass ejection (CME) with an average speed of about 1590 km s^{-1} that was measured in the online CME catalog of the *Coordinated Data Analysis Workshop* (CDAW) (cdaw.gsfc.nasa.gov/CME_list/: Yashiro et al., 2004) at a position angle of 28°. The site where the eruption started (and the associated flare occurred) was behind the limb for observations from the Earth's direction.

The flare site was not occulted for the *Sun Earth Connection Coronal and Heliospheric Investigation* instrument suite (SECCHI: Howard et al., 2008) on the Ahead spacecraft of the *Solar-Terrestrial Relations Observatory* (STEREO: Kaiser et al., 2008) that was located 35.0° eastward from the Earth. Figure 1a presents the view from the *Extreme UltraViolet Imager* (EUVI: Howard et al., 2008) onboard STEREO-A to the filament eruption and the flare site in 195 Å. According to the STEREO-A/EUVI observations in 195 Å and in 304 Å, the filament eruption started at about 04:15. The estimated position of the flare site as seen from Earth is N32 E116. The intense flare emission caused a strong overexposure distortion (blooming) that appears in Figure 1a as a bright, thick saturation streak. The method proposed by Chertok, Belov, and Grechnev (2015) allows for estimating the flare size of $\gtrsim$ M4 from the length of the blooming streak. This is a lower estimate because the streak is multi-element.

The *Atmospheric Imaging Assembly* (AIA: Lemen et al., 2012) onboard the *Solar Dynamics Observatory* (SDO: Pesnell, Thompson, and Chamberlin, 2012) observed the ejecta rising above the limb starting at 04:21:30. Figure 1b shows an SDO/AIA image obtained in 304 Å; the ejecta looks mostly the same in the six AIA channels that are dominated by iron emission lines. The cross in the lower-right corner denotes the projected position of the flare site.

The event was also observed at 5.8 – 11.8 GHz by the SRH middle-frequency interferometer operating in the test mode. Since late 2021, the low-frequency and middle-frequency SRH interferometers have started sessions of test observations, while their interruptions occurred for additional testing. Figure 1c shows a "clean" image of the ejecta obtained by SRH at 11.8 GHz. The blue contour in the lower-left corner represents the SRH beam at half level. It was $10'' \times 37''$ at that time at 11.8 GHz and inversely proportional to the observing frequency. The ejecta looks basically the same in the SRH images produced at different

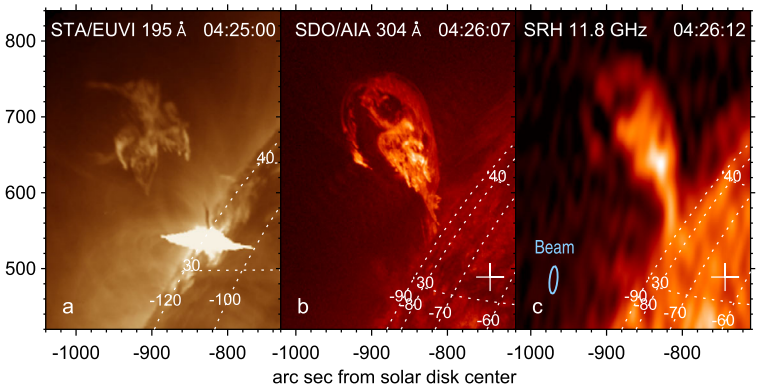

Figure 1 The filament eruption observed by STEREO-A/EUVI in 195 Å (**a**), by SDO/AIA in 304 Å (**b**), and by SRH at 11.8 GHz (**c**). The *blue contour* in the lower-left corner of panel **c** represents the SRH beam at half level. The *cross* at about N32 E64 in panels **b** and **c** denotes the projected position of the flare site. The *heliographic grid* on all panels corresponds to zero longitude as viewed from Earth.

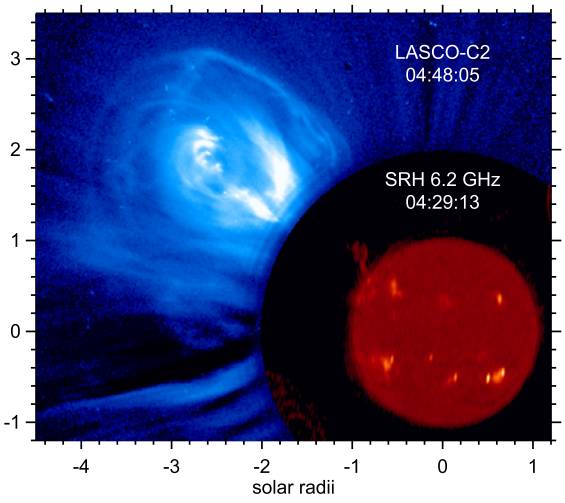

Figure 2 Full-disk image of the Sun with the erupting filament observed by SRH at 6.2 GHz (*lower-right part, red black-body colors*) and the CME observed 19 minutes later by LASCO-C2 (*upper-left part, blue*). The *axes* show the distances from the solar disk center in solar radii.

frequencies. The main differences are determined by the spatial resolution, i.e., the SRH beam size. Therefore, the spatial structure of the ejecta is better distinguishable at the highest available frequency; in addition, it is easier to visually assess the accuracy of tracking the regions of interest. For these reasons, we show images produced by the SRH at 11.8 GHz. Despite the considerably poorer spatial resolution compared to AIA, the 11.8 GHz SRH image reproduces the structural details of the ejecta and its surroundings.

Figure 2 presents an example of a full-disk image of the Sun with an erupting prominence above it produced by SRH at 6.2 GHz combined with a CME image observed by SOHO/LASCO-C2 19 minutes later. Two circumstances favored SRH observations of this event. First, the absence of the flare emission due to the far-side location of the flare site saved the SRH dynamic range to measure the ejecta accurately. Second, as the inset in Figure 2 shows, the SRH field of view where the ejecta occurred (up to 2.5 $R_{\odot}$) did not overlap at that time with adjacent images, which are inherent for the response of equidistant interfer-

ometers. Both occultation of the flare site and the absence of overlap with adjacent images favor measuring the brightness temperatures of the ejecta against the clear sky.

The ejecta is detectable in SRH images up to about 2 $R_\odot$. Shortly after the appearance from behind the limb, its near-the-limb portion observed at a height of $\lesssim 0.07$ $R_\odot$ around 04:24 was weakly polarized (e.g., 2.5% at 6.2 GHz). The body of the erupting filament did not show any detectable polarization later on.

2.2. Kinematics of the Eruption and Tracking Its Piece

The initial pre-eruptive filament was small and located behind the limb. The translational movement of the filament is accompanied by its three-dimensional expansion in all directions and rotation. In the first, rough approximation, the expansion is self-similar (strictly speaking, the self-similar approximation does not apply at the impulsive acceleration stage; see Uralov, Grechnev, and Hudson, 2005). In this approximation, filament pieces expand radially from the virtual expansion center. The expansion center of a small active-region filament is generally close to its initial position (flare site), which determines its super-radial expansion. In the case of a large filament eruption outside of active regions, the expansion center is shifted from the eruption site to the center of the Sun so that the filament expansion is closer to radial. In this event, the use of the projected position of the flare site (the cross in Figures 1b and 1c) as the expansion center provided satisfactory results.

If the kinematics of the erupting filament is known, then its expansion can be compensated for by resizing the field of view of the images, keeping the position and apparent size of the ejecta fixed. In such images, it is easier to follow the selected moving and expanding piece accurately. The quality of the measurements is assessed by the visual inspection of a movie composed from such scaled images, where the structure in question should be static. The AIA193_304_SRH_eruption.mpg file in the Electronic Supplementary Material presents this movie.

The initial part of the kinematic plots was measured from STEREO-A/EUVI images and then continued from SDO/AIA images. We manually fitted the accelerations for the leading edges of the erupting structures with four Gaussian pulses and adjusted their parameters to obtain the best fit. The parameters were refined in sequential attempts. The distance–time measurements from AIA images were coordinated with the images produced by the *Large Angle Spectroscopic Coronagraph* (LASCO: Brueckner et al., 1995) onboard the *Solar and Heliospheric Observatory* (SOHO: Domingo, Fleck, and Poland, 1995).

Our measurements for the leading edge of the ejecta match the CME front in LASCO-C2 images. However, it is difficult to identify the elements of the CME core with the internal structure of the erupting filament that considerably changed during the temporal gap between the AIA and LASCO observations. The results of the measurements are shown in the two next figures; Figure 3 shows four SDO/AIA 195-Å images of the ejecta that were resized according to the measured kinematic plots presented in Figure 4.

Figure 3 and the AIA193_304_SRH_eruption.mpg movie in the Electronic Supplementary Material demonstrate that the ejection had a complex structure, whose expansion was mostly close to self-similar, but not exactly in detail. The foremost configuration outlined by the solid arc consisted of several loops, whose apparent southeastern end slowed down relative to the leading edge. The twisted structure following it, outlined by the dashed arc, appeared from behind the limb later but expanded more vigorously, bent, and tended to approach the leading edge. These particularities complicate tracking selected pieces of the erupting filament and require additional adjustment of the kinematic plots used for this purpose, including time-dependent direction corrections.

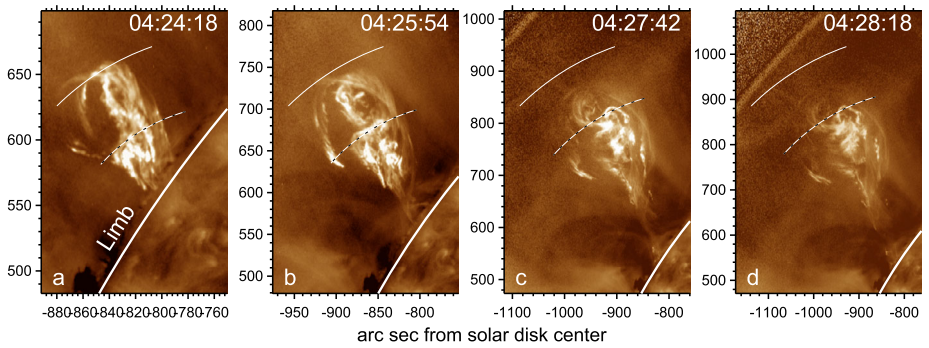

Figure 3 Four SDO/AIA 195-Å images of the ejecta with a field of view resized according to the measured kinematics shown in Figure 4a. The *thin-solid arc* outlines the leading edge of the whole ejecta. The *thin-dotted arc* outlines the leading edge of the twisted structure. The *thick-solid arc* represents the optical limb.

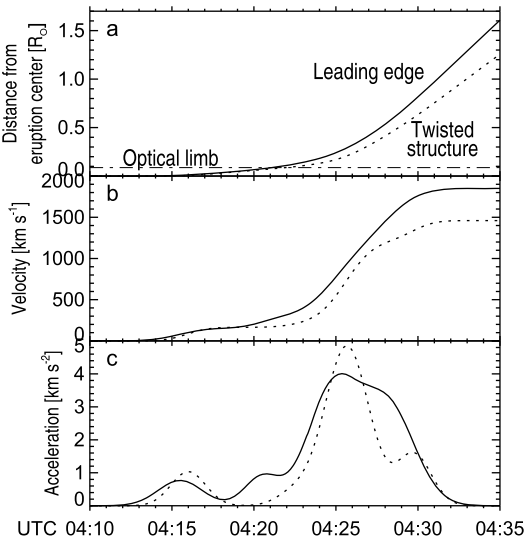

Figure 4 Kinematics of the erupting filament measured from STEREO-A/EUVI and SDO/AIA images. The *solid curves* correspond to the leading edge of the whole ejecta, and the *dotted curves* correspond to its inner twisted structure.
a) Distance–time plot measured from the projected position of the eruption center. The *horizontal dash-dotted line* represents the optical limb. **b**) Velocity–time plot. **c**) Acceleration–time plot.

3. Free-Free Radio Emission and Polytropic Scaling of a Rapidly Expanding Prominence Plasma

3.1. Assumptions and Restrictions

We assume that the plasma of an erupting prominence conditionally consists of two spatially noncoinciding components: hot, almost completely ionized, and cold, partially ionized. The hot component is responsible for the emission of EUV lines during the eruption, while the cold component is responsible for the commonly observed screening of solar EUV radiation by a quiet prominence. This separation is motivated by the assumption that the hot component, in contrast to the cold one, is penetrated by magnetic-field lines that participate in magnetic reconnection at the prominence activation and eruption stages.

The absence of a detectable polarization almost all the time of observation and the large height of the eruption above the photosphere suggest that the magnetic field was weak and

rule out in the microwave range both gyromagnetic emission of thermal or non-thermal electrons and plasma emission because of the low plasma density. Only the emission mechanism of thermal electrons in collisions with ions and neutral atoms remains. The corresponding absorption coefficients depend on the plasma parameters, $\mu_{ei} \propto n_e n_i T^{-3/2}$ and $\mu_{en} \propto n_e n_n T^{1/2}$, where T is the plasma temperature, and n_e, n_i, and n_n are the number densities of electrons, ions, and neutrals, respectively (e.g., Zheleznyakov, 1970, 1996; Loukitcheva et al., 2004; Heinzel et al., 2015). In the case of hydrogen plasma, $n_e = n_i$, the ratio of absorption coefficients is determined by temperature and the degree of hydrogen ionization and is numerically $\mu_{ei}/\mu_{en} \approx 10^2 T^{-2} n_e/n_n$. In turn, the degree of ionization depends in a complex way on temperature, pressure, and the location of the plasma element in the solar atmosphere. In stationary models of the solar chromosphere, the n_e/n_n ratio is calculated under the assumption of non-local thermodynamic equilibrium (non-LTE).

Such an equilibrium occurs as a balance between photoionization, radiative recombination, and collisional recombination/ionization. Therefore, a change in the temperature and density of the cold-component plasma during the expansion of the erupting prominence should, it would seem, lead to a change in the degree of hydrogen ionization. The expansion of hydrogen plasma can no longer be strictly polytropic in the range of temperatures and densities, where changes in the degree of ionization are significant. This would also lead to a complication in the theoretical estimation of the optical thickness. This would occur in a slow, quasi-stationary expansion of the erupting plasma, when the relaxation time for ionization equilibrium or the ionization/recombination timescale $[\Delta t_{ioniz}]$ is much shorter than the characteristic expansion time or dynamical timescale $[\Delta t_{exp}] = n_e/|\mathrm{d}n_e/\mathrm{d}t| = r/3u$ (this follows from the dependence $n_e \propto r^{-3}$). Here, $u = \mathrm{d}r/\mathrm{d}t$ is the velocity of the plasma piece of the erupting structure, and r is its distance from the eruption center. In the self-similar expansion, $u \propto r$ and therefore Δt_{exp} is the same in all elements of the eruption at each moment of time. In the situation under discussion, expansion is proceeding rapidly. In the distance range $r = (0.2-0.5)\ \mathrm{R}_\odot$, Δt_{exp} is about 75 s. A similar value is easily found from Figure 4. For example, when the speed of the leading edge of the whole ejecta and its inner twisted structure was 1000 $\mathrm{km\,s^{-1}}$, their distance to the expansion center was $r = 0.3\ \mathrm{R}_\odot$. These values correspond to $\tau_{exp} = 70$ s. It is worth noting that during the interval of sharp acceleration we are discussing, the indicated value of τ_{exp} changes little, since within this interval approximately $u \propto r$ (see Figure 4). However, after completing the acceleration stage and entering the expansion regime at a constant speed, the expansion time grows, $\tau_{exp} \propto r$.

On the other hand, it is possible to estimate the actual value for Δt_{ioniz} in our event using the plasma parameters found in Section 3.3. For the pressure of the cold plasma component $p \approx 10^{-3}$ dyne cm^{-2} and at temperature $T \approx 10^4$ K, we find from Figure 6 in Chae (2021) that Δt_{ioniz} well exceeded 130 s (see also Carlsson and Stein, 2002).

The main contribution to microwaves in our brightness temperature measurements comes from the cold component of the erupting-prominence plasma. At the beginning of the eruption, this component is similar to the chromospheric plasma and contains the bulk of the prominence mass. As the analysis of the millimeter-wave radio emission from quiescent prominences and the quiet chromosphere above the temperature minimum shows, the radio-opacity is dominated by electron-proton collisions, $\mu_{ei} \gg \mu_{en}$ (e.g., White, Loukitcheva, and Solanki, 2006; Heinzel et al., 2015, 2022; Rodger and Labrosse, 2017). The above condition $\Delta t_{exp} < \Delta t_{ioniz}$ (or even $\Delta t_{exp} \ll \Delta t_{ioniz}$) indicates that the degree of hydrogen ionization with a rapid decrease in temperature and density of dynamic plasma lags considerably behind the ionization degree, which would correspond to the ionization equilibrium of static plasma at the same values of temperature and density and photoionizing radiation field. Bearing in mind this factor of ionization inertia and the fact that the interval of our

microwave measurements (about 04:24 – 04:30 in Figure 4) does not exceed much, if not commensurate with the value of $\Delta t_{\rm ioniz}$, when estimating the polytropic index, we assume that the $n_{\rm e}/n_{\rm n}$ ratio does not change. An indirect indication of the validity of such an assumption will be found in the analysis of experimental data in Section 3.3.

Grechnev et al. (2019) studied the high-temperature component of the erupting-prominence plasma in an event very similar to the event in question. The contribution of the hot component to the microwave emission is negligible, since the brightness temperature of the optically thin plasma is low and decreases with increasing kinetic temperature. Note the circumstances of the event studied by Grechnev et al. (2019) that are probably related to our event. The temperature of the hot component increased as the erupting prominence rose to $\approx 0.2\ {\rm R}_\odot$. The hot erupting structures were heated up to ≈ 10 MK, presumably by accelerated electrons injected from the reconnection site. The rapid heating and expansion of that ejection led to the onset of the freeze-in process for the Fe-ion charge state at the early stage of expansion of the erupting prominence. In that case, the ionization state of the lower-temperature $Fe^{8+} - Fe^{14+}$ ions became frozen-in at distances $\gtrsim 2\ {\rm R}_\odot$, while that of the higher-temperature $Fe^{15+} - Fe^{23+}$ ions froze-in earlier, within $2\ {\rm R}_\odot$. In this regard, it seems possible that during the impulsive acceleration stage of the cold plasma component, the degree of hydrogen ionization in our event also tends to freeze-in, since the ionization/recombination timescale for hydrogen is longer than the dynamical timescale. However, this trend does not mean that the ionization freeze-in conditions have actually been achieved. Empirical modeling of the charge-state evolution of different elements of cold and hot plasma components of an eruptive prominence predicts that the ionization states of some ions are still not in the freeze-in state even at large distances, and freezing conditions are more easily achieved for ions of the hot component of the ejected plasma (see, e.g., Rivera et al., 2019 and references therein).

3.2. Expected Brightness-Temperature Variations in an Expanding Ejecta

In the case of thermal free-free emission of electrons in collisions with protons, the brightness temperature $[T_{\rm b}]$ of an erupting plasma piece with a geometric thickness $[l]$, a uniform distribution of kinetic temperature T, and electron number density $n_{\rm e}$ is estimated as follows:

$$T_{\rm b} = (1 - e^{-\tau})T; \quad \tau = A_{\rm ff}\frac{n_{\rm e}^2\lambda^2}{T^{3/2}}l. \tag{1}$$

Here, τ is the optical thickness calculated in the approximation corresponding to our situation when the observing frequency $[\nu]$ far exceeds the plasma frequency; $A_{\rm ff}$ is a dimensional coefficient, which is a constant in our consideration; $\lambda = c/\nu$ is a wavelength, and c is the speed of light. The value of $T_{\rm b}$ calculated from Equation 1 does not necessarily coincide with $T_{\rm b}^{\rm obs}$ measured in the experiment. The reasons may be the "raggedness" of the ejecta and the size of the beam pattern of the radioheliograph, expressed in steradians, $\Omega_{\rm beam} \propto \lambda^2$. With a size $[\Omega]$ of the feature in question, its observed and real brightness temperatures are related as $T_{\rm b}^{\rm obs}(\Omega + \Omega_{\rm beam}) = T_{\rm b}\Omega$. This equality means that the radiation flux is preserved when convolving the Gaussian intensity distribution in a source with a beam pattern that is also approximated by a Gaussian function. The value of Ω rapidly increases as the eruption expands away from the limb. In the present study, the value of $\Omega_{\rm beam}$ is appreciably less than Ω in the measurement region far enough from the limb. Therefore, we will not distinguish between $T_{\rm b}^{\rm obs}$ and $T_{\rm b}$ for now.

To calculate T_b, it is necessary to set the patterns of change in the quantities that determine, according to Equation 1, the optical thickness τ of a plasma piece, whose volume $[V]$ changes. We postulate the conservation of the total number of particles $N = (n_e + n_i + n_n)V$ and their ratios in this volume. Together with the polytropic expansion law, this leads to the dependence

$$n_e = n_{e0}(V_0/V),\ p = p_0(V_0/V)^{\alpha},\ T = T_0(V_0/V)^{\alpha-1},\ p = NkT/V. \tag{2}$$

Here, k is the Boltzmann constant, and subscript "0" marks the values of quantities corresponding to the measured part of the ejecta when it is located at a distance of r_0 from the expansion center. These quantities are its size l_0 along the line of sight, volume V_0, as well as pressure, temperature, and plasma density. The specific value of the distance r_0 and the values of the quantities with subscript "0" do not matter since they fall out of consideration when obtaining the main results of our study. From Equation 2, it follows the pattern of optical–thickness variation:

$$\tau = \tau_0(V_0/V)^{2-\frac{3}{2}(\alpha-1)}(l/l_0), \quad \tau_0 = A_{ff}\frac{n_{e0}^2\lambda^2}{T_0^{3/2}}l_0. \tag{3}$$

In the self-similar approximation (see, e.g., Sedov, 1977; Low, 1982; Uralov, Grechnev, and Hudson, 2005), we have

$$V_0/V = (r_0/r)^3, \quad l/l_0 = r/r_0. \tag{4}$$

In this case, the optical thickness (Equation 3) and kinetic temperature (Equation 2) of the selected eruption piece change with distance as follows:

$$\tau = \tau_0(r_0/r)^{(19-9\alpha)/2}, \quad T = T_0(r_0/r)^{3\alpha-3}. \tag{5}$$

Substituting Equation 5 into Equation 1 gives the dependence of the brightness temperature of radiation from a plasma piece on its distance from the expansion center, $T_b(\nu, r)$. The plot of this dependence consists of two branches, which are power-law functions corresponding to the optically thick ($\tau \gg 1$) and optically thin ($\tau \ll 1$) limits of the emission source. In each of these cases,

$$T_b = T = T_0(r_0/r)^{3\alpha-3} \equiv T_0(r/r_0)^{-\delta_1}, \quad \tau \gg 1; \tag{6}$$

$$T_b = \tau T = \tau_0 T_0(r_0/r)^{(13-3\alpha)/2} \equiv \tau_0 T_0(r/r_0)^{-\delta_2}, \quad \tau \ll 1. \tag{7}$$

In log–log coordinates ($\log T_b$, $\log r$), the $T_b(\nu, r)$ dependence generally looks like a curve with a break in the vicinity of the intersection at $\tau \approx 1$ of two straight lines that are tangent to this curve at small and large values of r. The tangents correspond to the power-law functions represented by Equation 6 and Equation 7. Their exponents, δ_1 and δ_2, and the polytropic index α are related to each other in the following manner:

$$\delta_1 = 10 - 2\delta_2, \tag{8}$$

$$\alpha = 1 + \delta_1/3 = (13 - 2\delta_2)/3. \tag{9}$$

Note that the relation between T_b and the true value of the radiating-plasma temperature T is affected by the filling factor in the plane of the sky $[F]$. This factor is determined by the

ratio of the true angular area of small structural radiating elements of an eruptive prominence inside the interferometer beam pattern to the area of the pattern itself. The higher the angular resolution, the closer to unity the value of F can be. It is easy to take formal account of the filling factor by replacing $T \to TF$ in Equation 1, but the value of F itself is unknown. EUV images indicate that F must be taken into account if one wants to estimate the true value of the average plasma temperature from Equation 1. Under the assumption of self-similarity, the filling factor F does not change with expansion as long as the fine structures are still much smaller than the beam pattern, which seems to be the case in our observations. When estimating the polytropic index, this factor can be ignored since it falls out of consideration. Therefore, it is sufficient to find the dependence of $T_{\mathrm{b}}^{\mathrm{obs}}(r)$ for an element of the erupting prominence on the distance r.

Another methodological remark concerns the pattern of the plasma-density variation in the expanding prominence. It follows from Equations 2 and 4 that $n_{\mathrm{e}} \propto r^{-3}$. This circumstance indicates the difference in the patterns of the plasma-density variation with distance in the stationary solar wind and a nonstationary CME. For example, the solar-wind flow at a constant speed corresponds to the pattern $n_{\mathrm{e}} \propto r^{-2}$. Because of this, the expansion of a CME into the solar wind is accompanied by the formation of a low-density magnetic cloud. The pattern of the plasma-density variation $n_{\mathrm{e}} \propto r^{-3}$ during the CME formation is a consequence of the conservation of the shape and mass of the rising prominence. The mass conservation is determined both by the freezing of the magnetic field into the CME plasma and the impossibility of the plasma flowing along magnetic-filed lines back into the chromosphere due to the action of gravity (draining effect) because the acceleration of the ejection itself is an order of magnitude higher than the gravity acceleration in the observation interval we are discussing.

3.3. Experimental Polytropic Index

To find regions where heating was possible, we examined different parts of the ejecta. We refined tracking of selected structural features on high-resolution AIA 195-Å images and computed average brightness temperatures from background-subtracted SRH images within the regions comprising these features.

Figure 5 presents four pairs of SRH images obtained at 11.8 GHz (top) and nearly simultaneous SDO/AIA 195-Å images (bottom). In each SRH image, the pre-event background image was subtracted. To reveal the ejecta at large distances, we divided each AIA image by a radial filter computed as the azimuthally-averaged result of the circular scanning with a progressively increasing radius. The average brightness temperatures were computed within two selected regions. These were region 1 outlined with the solid contour and region 2 outlined with the broken contour. The contours acceptably hold both regions, although their location relative to each other conspicuously changed as the ejecta expanded.

The measurements were made using different image sets that SRH produced at different frequencies. We used "dirty" images synthesized at two frequencies of 5.8 and 6.2 GHz that were averaged to enhance the sensitivity. The equivalent reference frequency is 6.0 GHz. We also used "clean" images at 11.8 GHz. Figure 6 presents the results of the measurements made at the two frequencies of 6.0 and 11.8 GHz.

At short distances ($r \lesssim 0.3\ \mathrm{R}_{\odot}$), the two regions are not reliably separated. On the other hand, the SRH sensitivity of about 10^3 K puts a limit on measurements at relatively long distances. The measurements at moderate distances fall well on the broken double power-law pattern. However, there are imaging issues; for example, the outlier (triangle at $r \approx 0.43\ \mathrm{R}_{\odot}$ in Figure 6b) was caused by the overlap of region 2 with a residual side lobe from an adjacent negative interference maximum. We ignored this outlier.

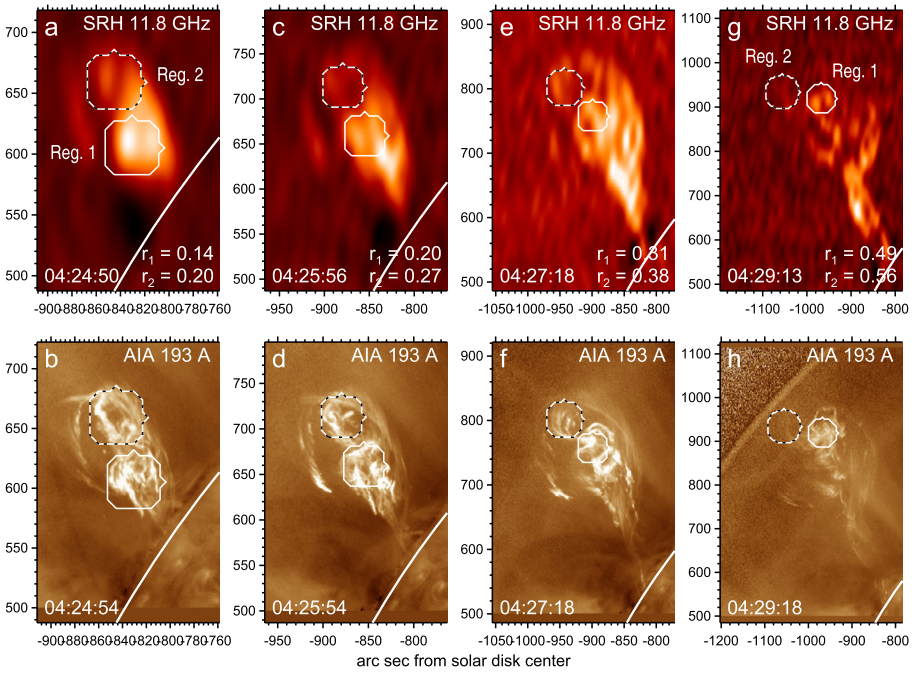

Figure 5 Four SRH 11.8 GHz images (top) and nearly simultaneous SDO/AIA 195-Å images (bottom) of the ejecta with a field of view scaled to compensate for its expansion. The *contours* outline region 1 (*solid*) and region 2 (*broken*), where the average brightness temperatures were measured in the SRH images. The distances between the expansion center and the centers of regions 1 and 2 are indicated in the lower-right corners of the SRH images. The *thick-solid arc* represents the optical limb.

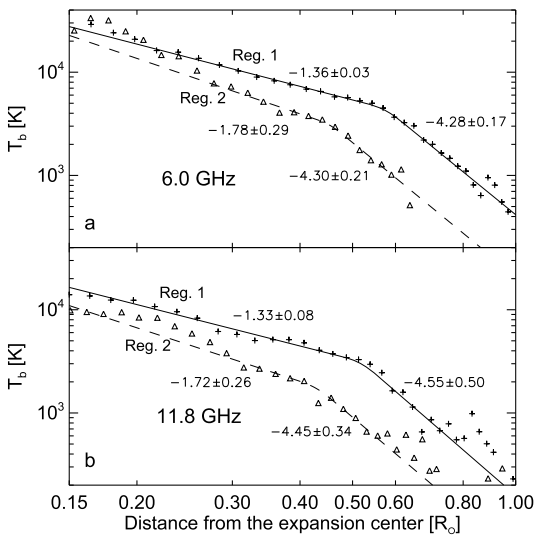

Figure 6 Brightness temperature vs. distance distributions measured from SRH images at two frequencies of 6.0 GHz (**a**) and 11.8 GHz (**b**) for region 1 (*crosses*) and region 2 (*triangles*). The *solid* and *dashed* lines represent their fitting with a broken double power-law.

As an example, we consider the $T_b(\nu, r)$ plot for region 1 at 6.0 GHz (Figure 6a). Its optically thick part corresponding to small distances r exhibits $\delta_1 = 1.36 \pm 0.03$, and the optically thin part to the right from the break exhibits $\delta_2 = 4.28 \pm 0.17$. There is fair correspondence (in terms of standard deviations) between δ_1 and δ_2 through Equation 8. The value $\delta_1 = 1.36$, measured with the smallest relative deviation, should correspond to $\delta_2 = 4.32$ within the confidence interval of measurements. A similar correspondence between δ_1 and δ_2 is maintained in all of the four $T_b(\nu, r)$ plots in Figure 6. These correspondences can be interpreted as an indirect confirmation of the assumption about the constancy of the ratios between the numbers of electrons, ions, and neutrals in a rapidly expanding ejected plasma.

The values of δ_1 measured at the two frequencies for region 1 have the smallest relative deviations. Substituting their average value into Equation 9 gives the polytropic index $\alpha \approx 1.45$. (The measurements for region 2 have a larger scatter. Here δ_2 have the smaller relative deviations, giving a close value of $\alpha \approx 1.42$.) The question arises as to what the value of $\alpha \approx 1.45$ means. This issue is addressed in the next section.

Here, we note the following circumstances. The break in the $T_b(\nu, r)$ plots in Figure 6 corresponds to $\tau \approx 1$ and, according to Equation 1, to $T_b \approx 0.63T$. This fact could be used to directly estimate the temperature of the cold plasma component of the erupting prominence at this moment without questionable assumptions about its dimensions and electron density. However, the need to take into account the unknown filling factor F reduces the importance of such a diagnostic tool. The observed $T_b(\nu, r)$ plots can be converted into true brightness temperatures of fine-structure elements of the prominence by multiplying $T_b(\nu, r)$ by F^{-1}. Therefore, the brightness temperatures at the breakpoints of the $T_b(\nu, r)$ plots in Figure 6 of 2×10^3 K $\leq T_b(\nu) \leq 4 \times 10^3$ K and, accordingly, the plasma temperatures of 3.2×10^3 K $\leq T \leq 6.3 \times 10^3$ K, represent the lower limit of the true values. The break condition, $\tau \approx 1$, for regions 1 and 2 in Figure 5 is satisfied at distances $r \approx 0.5$ R$_\odot$ from the expansion center, i.e. at heights exceeding ≈ 0.5 R$_\odot$ above the solar surface.

Let us estimate the column emission measure EM using Equation 1 for τ. For temperatures $T < 3 \times 10^5$ K, the A_{ff} factor is $A_{ff} \approx 2 \times 10^{-23} \ln\left(10^4 T^{2/3} n_e^{-1/3}\right)$ (e.g., Zheleznyakov, 1970). The logarithmic factor here is the Coulomb logarithm, which is about 10 for $T \approx 10^4$ K and a reasonable range of $n_e \approx (10^8 - 10^9)$ cm^{-3}. The Coulomb logarithm does not depend on the emission frequency ν and is determined by the plasma frequency and thermal electron velocity. In a more refined high-frequency representation of the A_{ff} factor, instead of the Coulomb logarithm, the Gaunt factor is used (see Ginzburg, 1970; Dulk, 1985; Huba, 2004). The Gaunt factor does not depend on the plasma frequency but depends on the emission frequency ν and plasma temperature T. It is important that in both cases, the values of the A_{ff} factor are close in magnitude, showing a weak logarithmic dependence on plasma parameters that change with expansion, namely temperature and density. We neglected this weak dependence in Equation 3 as insignificant within the accuracy of our measurements of the pattern of optical-thickness variation of the event in question.

From the condition $\tau \approx 1$ at our frequencies of about 10 GHz, we find EM $= n_e^2 l \approx 2 \times 10^{26}$ cm^{-5} with a characteristic dimension of the erupting prominence in Figure 5g of $l \approx 100''$. Hence $n_e \approx 2 \times 10^8$ cm^{-3} and plasma pressure is $p \approx 2 n_e k T \approx 6 \times 10^{-4}$ dyne cm^{-2}.

4. Discussion

4.1. Amount of Heat Released in Expansion of the Erupting Plasma

If the polytropic index α is equal to the adiabatic index $\gamma = 5/3$, then when the plasma expands from volume V_0 to volume V, the total heat inflow or outflow $[Q]$ is equal to zero.

If $\alpha < \gamma$ (or, vice versa, $\alpha > \gamma$), then according to Equation 2, the plasma temperature decreases with expansion slower (or faster) than in the case of adiabatic expansion. This means heat inflow from the outside, $Q > 0$ (or heat outflow, $Q < 0$). In compression, the situation is reversed in both cases. Let us now evaluate what has been said.

In the adiabatic expansion of the plasma volume, its internal energy $[\varepsilon]$ is spent on performing work $[w]$ against external forces, $\Delta\varepsilon - w = 0$. Violation of this relation obeys the first law of thermodynamics for the amount of heat Q transferred to the plasma volume:

$$Q = \Delta\varepsilon - w. \tag{10}$$

For the polytropic expansion, $pV^{\alpha} = p_0 V_0^{\alpha} = b$ with b being a constant, we obtain from Equation 2:

$$w = -\int_{V_0}^{V} pdV = \frac{b}{\alpha - 1}\left(V^{1-\alpha} - V_0^{1-\alpha}\right); \tag{11}$$

$$\Delta\varepsilon = NC_v(T - T_0) = \frac{bC_v}{k}\left(V^{1-\alpha} - V_0^{1-\alpha}\right). \tag{12}$$

As a result, the amount of heat released during the polytropic change in the plasma volume from V_0 to V is given by the expression

$$Q = b\left(\frac{C_v}{k} - \frac{1}{\alpha - 1}\right)\left(\frac{1}{V^{\alpha-1}} - \frac{1}{V_0^{\alpha-1}}\right). \tag{13}$$

Here, C_v is the heat capacity at constant volume, pertaining to all degrees of freedom of one particle of the heated plasma. Neglecting the contribution of molecules with more than three degrees of freedom, we further assume $C_v = 3k/2$. It is convenient to rewrite Equation 13 for one plasma particle, ion or electron:

$$q = Q/N = kT_0\left(\frac{3}{2} - \frac{1}{\alpha - 1}\right)\left(\left(\frac{V_0}{V}\right)^{\alpha-1} - 1\right). \tag{14}$$

The maximum inflow or outflow of thermal energy per particle of plasma expanding to infinity is equal to

$$q_\infty = \lim_{V\to\infty} q = kT_0\left(\frac{1}{\alpha - 1} - \frac{3}{2}\right) \quad \text{for} \quad \alpha > 1; \tag{15}$$

$$q_\infty = \infty \quad \text{for} \quad \alpha \le 1.$$

It follows from Equations 15 and 9 that the heating of the expanding plasma, $q_\infty > 0$, corresponds to the values $\alpha < \gamma = 5/3$ and, accordingly, $\delta_1 < 2$ and $\delta_2 > 4$. Cooling, $q_\infty < 0$, corresponds to the values $\alpha > \gamma$; $\delta_1 > 2$, and $\delta_2 < 4$. Under adiabatic expansion $q_\infty = q = 0$, $\alpha = \gamma$, $\delta_1 = 2$, and $\delta_2 = 4$.

The polytropic index $\alpha = 1.45$ found in Section 3.3 corresponds to $q_\infty = 0.72kT_0 > 0$. This means that a piece of an eruptive filament, when moving to infinity from the position r_0, will receive approximately half of the thermal energy $\varepsilon = 3NkT_0/2$, which it had at a distance r_0 from the expansion center. This conclusion is entirely due to the assumption that the polytropic index of the expanding plasma is constant. As shown in Section 3.3, this assumption holds in the altitude range of our measurements. Using this circumstance,

one can get a notion of the evolution of the heating rate $\mathrm{d}q/\mathrm{d}t$ in the plasma of an eruptive filament using the similarity relation described by Equation 4:

$$\mathrm{d}q/\mathrm{d}t = HkT_0\frac{u}{r_0}\left(\frac{r_0}{r}\right)^{3\alpha-2}, \quad H = 3\left(1-\frac{C_v}{k}(\alpha-1)\right), \quad u = \frac{\mathrm{d}r}{\mathrm{d}t}, \tag{16}$$

where u is the velocity, and H is the heating coefficient; $H = 0$ when the polytropic index α is equal to the adiabatic index $\gamma = (i+2)/i$; i is the number of degrees of freedom, and $C_v = ik/2$.

With $\alpha = 1.45$, it follows that:

$$\mathrm{d}q/\mathrm{d}t \approx kT_0\frac{u}{r_0}\left(\frac{r_0}{r}\right)^{2.35}. \tag{17}$$

In the limiting case of an instantaneous increase in velocity to u_0, the maximum value of $\mathrm{d}q/\mathrm{d}t$ is reached at the onset of motion, $(\mathrm{d}q/\mathrm{d}t)_{\max} \approx kT_0(u_0/r_0)$, and then it decreases as $(r/r_0)^{-2.35}$. The main heating of the cold plasma component in the eruptive prominence occurs at the initial stage of its expansion. A similar conclusion, necessary to account for the EUV emission lines, was obtained for the hot component of an eruptive prominence (e.g., Lee et al., 2017). Note that the heating can occur not only due to the imbalance of the heating and cooling rates in the plasma. An important factor in the violation of the heat balance may be the destruction of the plasma circulation that existed before the eruption along the magnetic threads that constituted the prominence.

The above example of an instantaneous increase in velocity to u_0 is a useful idealization. Our measurements in Figures 5 and 6 correspond to the temporal interval within the acceleration pulse in Figure 4. The first approximation that takes this circumstance into account is the assumption that each plasma element inside the expanding ejecta moves with its own constant acceleration $[a]$ (recall that the condition for the self-similar expansion is a linear spatial profile of both the velocity and acceleration of the plasma inside the ejecta, $a \propto u \propto r$). Substituting $u = at$ into Equation 16, we find

$$\mathrm{d}q/\mathrm{d}t = HkT_0\frac{\sqrt{2a(r-r_0)}}{r_0}\left(\frac{r_0}{r}\right)^{3\alpha-2}. \tag{18}$$

The greater the acceleration, the higher the heating rate. For $(r - r_0) \ll r_0$, the heating rate increases with the expansion, $\mathrm{d}q/\mathrm{d}t \propto \sqrt{a(r-r_0)}$, and reaches its maximum value at $r^* = \beta r_0$, where $\beta = [1 - 0.5/(3\alpha - 2)]^{-1}$. For $\alpha = 1.45$, we get $\beta = 1.27$. For $r \gg r^*$, the heating rate for accelerating expansion decreases slightly more slowly with distance than for a constant-speed expansion (Equation 17):

$$\mathrm{d}q/\mathrm{d}t = HkT_0\sqrt{\frac{2a}{r_0}}\left(\frac{r_0}{r}\right)^{3\alpha-2.5} \propto \left(\frac{r_0}{r}\right)^{1.85}. \tag{19}$$

In a real situation, the acceleration phase has an impulsive character, and there is a transition from the pattern described by Equation 18 to the pattern described by Equation 16. Herewith, the gage r_0 in Equation 16 should be replaced by the distance from which the expansion continues at a constant rate.

A necessary condition for the validity of Equations 16 and 18 is the constancy of the polytropic index of the expanding plasma. This option is not contradicted by the results of Section 3.3 that demonstrate the required correspondence between δ_1 and δ_2 in the interval of our measurements. The power-law dependency in Equation 19 will be used further to figure out the plasma-heating mechanism in a rapidly expanding prominence.

4.2. Preferred Heating Mechanism

In the stationary state, the temperature of the cold component of the prominence magneto-plasma is determined by the balance of a number of factors. These include radiative cooling, ohmic heating, turbulence and wave dissipation, the divergence of conductive flux, possible presence of a fraction of energetic particles and hot plasma outflow generated in places of quasi-stationary magnetic reconnection, as well as quasi-stationary plasma flows not related to reconnection, along magnetic-field lines rooted to the solar surface. This entanglement makes it difficult to understand what is the main source of heating of the prominence plasma and, possibly, the plasma of the solar corona.

The situation changes crucially in the event of an eruption. The relationship between these factors changes dramatically and a new, very significant factor appears, which is adiabatic cooling.

In our case, this factor dominates. The combined effect of adiabatic cooling and other heating sources determines the pattern of the temperature T decrease and, accordingly, the polytropic index α of the expanding plasma. Let us try to understand what could be the main source of plasma heating in the interval of our measurements when the acceleration and rapid expansion of the ejection occurred.

To shorten the set of possible options, we recall that we are talking about the cold component of the ejected plasma, which makes the main contribution to its microwave image. As stated in Section 3.1, the behavior of the hot component during the acceleration stage is the opposite, i.e., heating dominates over adiabatic cooling. At high temperatures, the role of thermal conductivity sharply increases, and the significance of ohmic heating decreases. The collisional heating by flare-accelerated electrons is the most probable reason for heating the expanding plasma to about 10 MK (Lin et al., 2002; Glesener et al., 2013; Grechnev et al., 2019). For the cold component of the ejected plasma, whose temperature only decreases with expansion, we exclude from consideration the presence of accelerated electrons as a heating factor. The influence of factors that maintain the heat balance due to the circulation of plasma flows that existed before the eruption should also be excluded from consideration because this circulation is destroyed.

The choice of suitable heating factors is possible due to the non-stationarity of the ejection phenomenon itself. The polytropic character of the change in the parameters of the expanding plasma makes it possible i) to estimate the rate at which the efficiency of each of the possible heating or cooling factors decreases as it expands and ii) to evaluate the possible polytropic indices under the assumption of the dominance of one of the heating factors and compare with the experimentally found. We will use procedures i) and ii) without speculative numerical estimates of the dissipative transport coefficients (see, e.g., Huba, 2004) and gradients of the corresponding quantities.

4.2.1. Ohmic Heating

Electric current is the main condition for the eruption of a prominence. The presence of current is also clearly indicated by the helical structure in Figure 1b. Ohmic heating is caused by collisions of electrons with ions (e-i) and with neutrals (e-n).

The heating rate per particle due to (e-i)-collisions is

$$(\mathrm{d}q/\mathrm{d}t)_{\mathrm{e-i}} \propto j^2/(n_{\mathrm{e}}\sigma_{\mathrm{e-i}}) \propto (\nabla \times \boldsymbol{B})^2/(n_{\mathrm{e}}T^{3/2}) \propto (B/r)^2/(r^{-3}r^{-4.5(\alpha-1)}) \propto r^{4.5\alpha-7.5}. \tag{20}$$

Here, j is the electric current density, and $\sigma_{\mathrm{e-i}} \propto T^{3/2}$ is the electrical conductivity (e.g., Braginskii, 1965), and it is taken into account that in magnetohydrodynamics $j \propto (\nabla \times \boldsymbol{B}) \propto$

(B/l). The magnetic field frozen into the expanding plasma changes during expansion as $B \propto {n_\mathrm{e}}^{2/3} \propto r^{-2}$. Here, Equations 2 and 4 are used for n_e and T and the characteristic size of l. If we equate the power-law dependencies $(\mathrm{d}q/\mathrm{d}t)_{\mathrm{e-i}}$ in Equation 20 and $\mathrm{d}q/\mathrm{d}t$ in Equation 19, then from the equality of the exponents, $4.5\alpha - 7.5 = -3\alpha + 2.5$, we find $\alpha_{\mathrm{e-i}} = 4/3$. The polytropic index would have such a value if i) heating was provided only by ohmic losses due to (e-i)-collisions; ii) the accelerated expansion of the erupting prominence remained self-similar. Note that the comparison of the exponents gives the pattern of $\mathrm{d}q/\mathrm{d}t$ only in absolute value and does not tell about its sign. For such a comparison to be valid, the condition $\mathrm{d}q/\mathrm{d}t > 0$ must be satisfied, since $(\mathrm{d}q/\mathrm{d}t)_{\mathrm{e-i}} > 0$ by definition of ohmic heating. This condition is satisfied because the heating coefficient in Equation 16 $H > 0$ at $\alpha = 4/3$ that determines the sign of $\mathrm{d}q/\mathrm{d}t$.

The value $\alpha_{\mathrm{e-i}} \approx 1.33$ is reasonably close to the observed value $\alpha \approx 1.45$. The estimation error for α from Equation 9 is comparable to the largest measurement error for δ_1 and δ_2 (Section 3.3), being about $\pm 0.17(2/3) = \pm 0.11$. None of the heating mechanisms discussed below shows such closeness. Finally, substituting the measured value $\alpha = 1.45$ into Equation 20 shows that the (e-i)-heating rate decreases with expansion as

$$(\mathrm{d}q/\mathrm{d}t)^{\mathrm{obs}}_{\mathrm{e-i}} \propto r^{-0.975}. \tag{21}$$

Further, we will see that (e-i)-ohmic heating of an expanding magnetoplasma retains its efficiency much longer than other heating mechanisms.

The heating rate per particle due to (e-n)-collisions is

$$(\mathrm{d}q/\mathrm{d}t)_{\mathrm{e-n}} \propto j^2/(n_\mathrm{e}\sigma_{\mathrm{e-n}}) \propto (\nabla \times \boldsymbol{B})^2 T^{1/2}/n_\mathrm{e} \propto (B/r)^2 r^{-3(\alpha-1)/2}/r^{-3} \propto r^{-3(\alpha+1)/2}. \tag{22}$$

Here, the electrical conductivity is $\sigma_{\mathrm{e-n}} \propto (n_\mathrm{e}/n_\mathrm{n})T^{-1/2} \propto T^{-1/2}$ under the assumption that the ratio $(n_\mathrm{e}/n_\mathrm{n})$ does not change. A significant difference from the previous situation is the increase in electrical conductivity with expansion. Having done the same procedures with Equation 22 as in the previous part of this section, we find $\alpha_{\mathrm{e-n}} = 8/3 \approx 2.67$ and

$$(\mathrm{d}q/\mathrm{d}t)^{\mathrm{obs}}_{\mathrm{e-n}} \propto r^{-3.675}. \tag{23}$$

The value $\alpha_{\mathrm{e-n}} > \gamma = 5/3$ means the outflow of heat, $\mathrm{d}q/\mathrm{d}t < 0$, when, by definition of ohmic losses, there is heat inflow, $(\mathrm{d}q/\mathrm{d}t)_{\mathrm{e-n}} > 0$. This contradiction may mean that, without involving additional and more significant cooling factors, it is impossible to reconcile two processes, adiabatic cooling and ohmic heating due to (e-n)-collisions, by a single polytropic law. The polytropic fit of the observational data that we use seems to be quite satisfactory. This is an indirect indication that the factor $(\mathrm{d}q/\mathrm{d}t)_{\mathrm{e-n}}$ is not dominant. The result of this section is also Equation 23 showing a very rapid decrease with expansion in the (e-n)-heating rate, if such heating was significant at all.

4.2.2. Thermal Conduction

In this case, the inflow or outflow of thermal energy per particle is

$$(\mathrm{d}q/\mathrm{d}t)_{\mathrm{TC}} \propto \nabla \cdot (\kappa \nabla T)/n_\mathrm{e} \propto T^{7/2} r^{-2} n_\mathrm{e}^{-1} \propto r^{-10.5\alpha+11.5}, \tag{24}$$

where $\kappa \propto T^{5/2}$ is the sum of the electronic and ionic thermal conductivities. Comparison of the power-law dependencies $(\mathrm{d}q/\mathrm{d}t)_{\mathrm{TC}}$ in Equation 24 and $\mathrm{d}q/\mathrm{d}t$ in Equation 19 results in $-10.5\alpha + 11.5 = -3\alpha + 2.5$; hence $\alpha_{\mathrm{TC}} = 1.2$ and the heating coefficient $H > 0$, which

corresponds to the heat inflow. This means that thermal conductivity could compete for the role of the dominant heating source. However, the difference of $\alpha_{\rm TC}$ from the measured value $\alpha \approx 1.45$ noticeably exceeds the corresponding deviation of $\alpha_{\rm e-i}$, and the thermal-conduction heating rate decreases with expansion as

$$(\mathrm{d}q/\mathrm{d}t)^{\rm obs}_{\rm TC} \propto r^{-3.725}, \tag{25}$$

which is considerably faster than for $(\mathrm{d}q/\mathrm{d}t)^{\rm obs}_{\rm e-i}$.

4.2.3. Radiative Cooling

In this case, the loss of thermal energy per one plasma particle is

$$(\mathrm{d}q/\mathrm{d}t)_{\rm rad} \propto n_{\rm e} n_{\rm p} L^{\rm cool}(T)/n_{\rm e} \propto r^{-3} L^{\rm cool}(T), \tag{26}$$

where $n_{\rm p}$ is the proton number density, and $L^{\rm cool}(T)$ is the radiative-loss function of the solar plasma, which decreases very sharply at $T < 16 \times 10^3$ K (e.g. Schure et al., 2009). At the discussed temperatures $T < 10^5$ K decreasing with plasma expansion, the $L^{\rm cool}(T)$ could be considered to decrease with distance, so that $(\mathrm{d}q/\mathrm{d}t)_{\rm rad}$ decreases faster than r^{-3}. The quantity $(\mathrm{d}q/\mathrm{d}t)_{\rm rad}$ could formally depend on the polytropic index α via the temperature T, which is represented by the radiative-loss function. However, $L^{\rm cool}(T)$ is not a simple power-law function, and one cannot speak of a polytropic expansion of the plasma with inconsistent factors of adiabatic and radiative cooling.

4.2.4. Turbulence and Wave Dissipation

With a sharply non-stationary expansion of the magnetoplasma of an erupting prominence with supersonic and, probably, super-Alfvénic speed, the idea of the periodicity of wave motions inside it loses its validity. Considering only an estimate of the dissipation rate, we will consider possible wave motions inside the expanding volume as an addition to the existing turbulent pulsations, if any.

The dissipation of energy (erg g^{-1} s^{-1}) of turbulent motion per 1 gram of magnetoplasma is estimated as in hydrodynamics (Landau and Lifshitz, 1987):

$$(\mathrm{d}Q'/\mathrm{d}t)_{\rm T} \approx \eta_{\rm T}\overline{(\nabla u_{\rm T})^2} \approx (l_{\rm T}u_{\rm T})\overline{u_{\rm T}^2}/l_{\rm T}^2 \approx u_{\rm T}^3/l_{\rm T} \propto (\mathrm{d}q/\mathrm{d}t)_{\rm T}. \tag{27}$$

Here, $u_{\rm T}$ is the characteristic turbulent velocity, and $l_{\rm T}$ is its characteristic spatial size. Overline means averaging; $\eta_{\rm T} \approx l_{\rm T}u_{\rm T}$ is turbulent viscosity, analogous to kinematic viscosity; $(\mathrm{d}q/\mathrm{d}t)_{\rm T} = (\mathrm{d}Q'/\mathrm{d}t)_{\rm T}/N'$ with N' the number of particles in 1 gram of plasma.

It is necessary to determine the pattern of $u_{\rm T}$ change during expansion. To do this, we use a relation similar to Equation 10:

$$\mathrm{d}Q_{\rm T} = \mathrm{d}\varepsilon_{\rm T} - \mathrm{d}w_{\rm T}. \tag{28}$$

Here, $\mathrm{d}w_{\rm T} = -P_{\rm T}\mathrm{d}V$ is the work of the turbulence pressure forces $P_{\rm T} \approx \rho\overline{u_{\rm T}^2}$. The total energy $[\varepsilon_{\rm T}]$ of turbulent pulsations in volume V is defined as $\varepsilon_{\rm T} \approx \rho V\overline{u_{\rm T}^2} = M\overline{u_{\rm T}^2}$, M is the plasma mass in the volume V that does not change during expansion, $\mathrm{d}(\rho V) = 0$. The energy density $\rho\overline{u_{\rm T}^2}$ is equal to the sum of the kinetic and potential energies and is a consequence of the well-known circumstance; the average kinetic and potential (including electromagnetic) energies of a system that performs small oscillations are equal to each other. Assuming

further that turbulent heating is negligible compared to adiabatic cooling, we put $\mathrm{d}Q_\mathrm{T} = 0$ in Equation 28 as a first approximation:

$$\mathrm{d}\varepsilon_\mathrm{T} - \mathrm{d}w_\mathrm{T} \approx (V\rho)\mathrm{d}\overline{u_\mathrm{T}^2} + \rho\overline{u_\mathrm{T}^2}\mathrm{d}V = 0. \tag{29}$$

Hence $\overline{u_\mathrm{T}^2} \propto V^{-1} \propto r^{-3}$ or $u_\mathrm{T} \propto r^{-3/2}$. Substituting this dependency into Equation 27, we find $(\mathrm{d}Q/\mathrm{d}t)_\mathrm{T}$ of the second approximation and the dependency we need

$$(\mathrm{d}q/\mathrm{d}t)_\mathrm{T} \propto u_\mathrm{T}^3/l_\mathrm{T} \propto r^{-5.5}, \quad l_\mathrm{T} \propto r. \tag{30}$$

Equations 27 and 30 are obtained from dimensional considerations using characteristic, non-dissipative scales u_T and l_T and do not depend on specific values of the classical dissipative coefficients of viscosity, thermal conductivity, or electrical conductivity. Nevertheless, they show the correct result. The turbulence of characteristic scales determines the flow of energy into the region of small-scale pulsations, where their energy is converted into heat.

The results of this section are as follows:

i) The considered mechanisms of heating or cooling of the erupting magnetoplasma lose their efficiency during expansion much faster than the ohmic dissipation due to electron-proton collisions. To verify this, it is sufficient to compare Equations 23, 25, 26, and 30 with Equation 21.
ii) The theoretical polytropic index $\alpha_{\mathrm{e-i}}$, corresponding to the predominance of ohmic dissipation due to electron-proton collisions, is closest to the experimentally measured value α. The fact that $\alpha_{\mathrm{e-i}} < \alpha$ means that in addition to this, the main heating factor, there are less important heating factors.

5. Summary and Concluding Remarks

Our measurements and analysis show that during the eruption, the prominence continues to heat up and receives the amount of heat (Equations 14, 15) comparable to its thermal energy at the beginning of the impulsive-acceleration stage. The preferred source of heat is the ohmic dissipation of electric currents, which are simultaneously the main driver of the magnetohydrodynamic instability of the entire eruptive configuration. The use of microwave emission to determine the polytropic index of an expanding thermal plasma in our case indicates that the conclusions about the dominant heating source apply to a relatively cold component with temperatures below coronal.

On the other hand, the conclusions of Glesener et al. (2013) and Grechnev et al. (2016, 2019) about the heating of erupting filaments refer mainly to the appearance and evolution of a hot component with coronal and higher temperatures. In that case, the analysis of observations based on the inversion of the differential emission measure (DEM) from SDO/AIA images (Glesener et al., 2013) supplemented their analysis by imaging spectroscopy based on the X-ray data provided by the *Reuven Ramaty High-Energy Solar Spectroscopic Imager* (RHESSI: Lin et al., 2002). The most probable dominant mechanism capable of rapidly heating the filament plasma to high temperatures is collisional heating by flare-accelerated electrons that are injected from the acceleration site predominantly into the envelope of the flux rope, whose formation from a pre-eruptive filament starts in the course of an eruptive flare.

Here, we used an independent different method that was based on microwave imaging observations. A necessary step in each method is to measure the kinematics of the erupting

structure. Because of the high speed, its displacements in different AIA channels that are used for the DEM inversion can be large enough to distort the results and should be compensated for. On the other hand, accurate tracking of a feature in question in microwave images is important. This task is complicated by the fact that the hotter portions of the filament fade away in microwave images faster than the cooler parts. In addition, the dynamic range of microwave images produced by a radio interferometer is considerably poorer than that of AIA. This is why we referred to AIA images when tracking the portions of the erupting filament to be measured in SRH images.

Despite the difference in the methods, all studies point to the heating of filaments during their expansion in flare-associated eruptions. The difference between the dominant mechanisms for the continued heating of the cold and hot plasma components in the prominence at the stage of its accelerated expansion is most likely due to their location on different magnetic-field lines and the presence or absence of a magnetic connection with the electron acceleration sites.

Supplementary Information The online version contains supplementary material available at https://doi.org/10.1007/s11207-023-02210-w.

Acknowledgments We are grateful to our colleagues from the Radio Astrophysical Department and the Radio Astrophysical Observatory in Badary. We thank A.A. Kochanov for discussions and assistance. We thank the anonymous reviewer for valuable comments that helped improve the original manuscript. The SRH data were obtained using the Unique Research Facility Siberian Solar Radio Telescope (ckp-rf.ru/catalog/usu/73606/).

We are grateful to the NASA/SDO and the AIA science teams; the NASA's STEREO/SECCHI science and instrument teams; and the team operating LASCO on SOHO. SOHO is a project of international cooperation between ESA and NASA. We appreciate the team maintaining the CME Catalog at the CDAW Data Center by NASA and the Catholic University of America in cooperation with the Naval Research Laboratory.

Author contributions A.M. Uralov proposed the basic method, interpreted the results, and wrote Sections 1, 3, and 4. S.V. Lesovoi and M.V. Globa acquired, calibrated, and preliminarily analyzed the SRH data that were used in this study. V.V. Grechnev made measurements, prepared figures, and wrote Sections 2 and 5. All authors discussed intermediate results and further actions at all stages of the study and reviewed the manuscript.

Funding This study was financially supported by the Ministry of Science and Higher Education of the Russian Federation.

Data Availability The datasets analyzed during the current study were derived from the following public domain resources:

Virtual Solar Observatory sdac.virtualsolar.org/

CDAW Data Center cdaw.gsfc.nasa.gov/

SOHO LASCO CME Catalog cdaw.gsfc.nasa.gov/CME_list/

Raw and preliminary SRH data computed automatically in real time are accessible via ftp://ftp.rao.istp.ac.ru/SRH/. The test-mode SRH data used in this study are available from the corresponding author on reasonable request.

Declarations

Competing interests The authors declare no competing interests.

References

Akmal, A., Raymond, J.C., Vourlidas, A., Thompson, B., Ciaravella, A., Ko, Y.-K., Uzzo, M., Wu, R.: 2001, SOHO observations of a coronal mass ejection. *Astrophys. J.* **553**, 922. DOI. ADS.

Altyntsev, A., Lesovoi, S., Globa, M., Gubin, A., Kochanov, A., Grechnev, V., Ivanov, E., Kobets, V., Meshalkina, N., Muratov, A., Prosovetsky, D., Myshyakov, I., Uralov, A., Fedotova, A.: 2020, Multiwave Siberian Radioheliograph. *Solar-Terr. Phys.* **6**, 30. DOI. ADS.

Braginskii, S.I.: 1965, Transport processes in a plasma. *Rev. Plasma Phys.* **1**, 205. ADS.

Brueckner, G.E., Howard, R.A., Koomen, M.J., Korendyke, C.M., Michels, D.J., Moses, J.D., Socker, D.G., Dere, K.P., Lamy, P.L., Llebaria, A., et al.: 1995, The Large Angle Spectroscopic Coronagraph (LASCO). *Solar Phys.* **162**, 357. DOI. ADS.

Carlsson, M., Stein, R.F.: 2002, Dynamic hydrogen ionization. *Astrophys. J.* **572**, 626. DOI. ADS.

Chae, J.: 2021, Ionization of hydrogen in the solar atmosphere. *J. Astron. Space Sci.* **38**, 83. DOI. ADS.

Chertok, I.M., Belov, A.V., Grechnev, V.V.: 2015, A simple way to estimate the soft X-ray class of far-side solar flares observed with STEREO/EUVI. *Solar Phys.* **290**, 1947. DOI. ADS.

Domingo, V., Fleck, B., Poland, A.I.: 1995, The SOHO mission: an overview. *Solar Phys.* **162**, 1. DOI. ADS.

Dulk, G.A.: 1985, Radio emission from the sun and stars. *Annu. Rev. Astron. Astrophys.* **23**, 169. DOI. ADS.

Filippov, B., Koutchmy, S.: 2002, About the prominence heating mechanisms during its eruptive phase. *Solar Phys.* **208**, 283. DOI. ADS.

Ginzburg, V.L.: 1970, *The Propagation of Electromagnetic Waves in Plasmas*, Pergamon Press, Oxford. ADS.

Glesener, L., Krucker, S., Bain, H.M., Lin, R.P.: 2013, Observation of heating by flare-accelerated electrons in a solar coronal mass ejection. *Astrophys. J. Lett.* **779**, L29. DOI. ADS.

Grechnev, V.V., Uralov, A.M., Zandanov, V.G., Baranov, N.Y., Shibasaki, K.: 2006, Observations of prominence eruptions with two radioheliographs, SSRT, and NoRH. *Publ. Astron. Soc. Japan* **58**, 69. DOI. ADS.

Grechnev, V.V., Uralov, A.M., Kochanov, A.A., Kuzmenko, I.V., Prosovetsky, D.V., Egorov, Y.I., Fainshtein, V.G., Kashapova, L.K.: 2016, A tiny eruptive filament as a flux-rope progenitor and driver of a large-scale CME and wave. *Solar Phys.* **291**, 1173. DOI. ADS.

Grechnev, V.V., Kochanov, A.A., Uralov, A.M., Slemzin, V.A., Rodkin, D.G., Goryaev, F.F., Kiselev, V.I., Myshyakov, I.I.: 2019, Development of a fast CME and properties of a related interplanetary transient. *Solar Phys.* **294**, 139. DOI. ADS.

Heinzel, P., Berlicki, A., Bárta, M., Karlický, M., Rudawy, P.: 2015, On the visibility of prominence fine structures at radio millimeter wavelengths. *Solar Phys.* **290**, 1981. DOI. ADS.

Heinzel, P., Bárta, M., Gunár, S., Labrosse, N., Vial, J.-C.: 2022, Prominence observations with ALMA. *Front. Astron. Space Sci.* **9**, 983707. DOI. ADS.

Howard, R.A., Moses, J.D., Vourlidas, A., Newmark, J.S., Socker, D.G., Plunkett, S.P., Korendyke, C.M., Cook, J.W., Hurley, A., Davila, J.M., et al.: 2008, Sun Earth Connection Coronal and Heliospheric Investigation (SECCHI). *Space Sci. Rev.* **136**, 67. DOI. ADS.

Huba, J.D.: 2004, NRL: Plasma formulary. Technical report, NRL/PU/6790–04–477, Naval Research Laboratory, Washington, DC.

Kaiser, M.L., Kucera, T.A., Davila, J.M., St. Cyr, O.C., Guhathakurta, M., Christian, E.: 2008, The STEREO mission: an introduction. *Space Sci. Rev.* **136**, 5. DOI. ADS.

Kucera, T.A., Landi, E.: 2008, Analysis of EUV, UV, and H-alpha emission from two very different prominences. In: *AGU Spring Meeting Abstracts* **2008**, SP43B. ADS.

Landau, L.D., Lifshitz, E.M.: 1987, *Fluid Mechanics*, Pergamon Press, Oxford.

Lantos, P., Raoult, A.: 1980, Prominences at centimetric and millimetric wavelengths. II. Radio diagnostic of the prominences. *Solar Phys.* **66**, 275. DOI. ADS.

Lee, J.-Y., Raymond, J.C., Reeves, K.K., Moon, Y.-J., Kim, K.-S.: 2017, Heating of an erupting prominence associated with a solar coronal mass ejection on 2012 January 27. *Astrophys. J.* **844**, 3. DOI. ADS.

Lemen, J.R., Title, A.M., Akin, D.J., Boerner, P.F., Chou, C., Drake, J.F., Duncan, D.W., Edwards, C.G., Friedlaender, F.M., Heyman, G.F., et al.: 2012, The Atmospheric Imaging Assembly (AIA) on the Solar Dynamics Observatory (SDO). *Solar Phys.* **275**, 17. DOI. ADS.

Lin, R.P., Dennis, B.R., Hurford, G.J., Smith, D.M., Zehnder, A., Harvey, P.R., Curtis, D.W., Pankow, D., Turin, P., Bester, M., et al.: 2002, The Reuven Ramaty High-Energy Solar Spectroscopic Imager (RHESSI). *Solar Phys.* **210**, 3. DOI. ADS.

Loukitcheva, M., Solanki, S.K., Carlsson, M., Stein, R.F.: 2004, Millimeter observations and chromospheric dynamics. *Astron. Astrophys.* **419**, 747. DOI. ADS.

Low, B.C.: 1982, Self-similar magnetohydrodynamics. I - The $\gamma = 4/3$ polytrope and the coronal transient. *Astrophys. J.* **254**, 796. DOI. ADS.

Pesnell, W.D., Thompson, B.J., Chamberlin, P.C.: 2012, The Solar Dynamics Observatory (SDO). *Solar Phys.* **275**, 3. DOI. ADS.

Rao, A.P., Kundu, M.R.: 1977, A study of filament transition sheath from radio observations. *Solar Phys.* **55**, 161. DOI. ADS.

Rivera, Y.J., Landi, E., Lepri, S.T., Gilbert, J.A.: 2019, Empirical modeling of CME evolution constrained to ACE/SWICS charge state distributions. *Astrophys. J.* **874**, 164. DOI. ADS.
Rodger, A., Labrosse, N.: 2017, Solar prominence modelling and plasma diagnostics at ALMA wavelengths. *Solar Phys.* **292**, 130. DOI. ADS.
Schure, K.M., Kosenko, D., Kaastra, J.S., Keppens, R., Vink, J.: 2009, A new radiative cooling curve based on an up-to-date plasma emission code. *Astron. Astrophys.* **508**, 751. DOI. ADS.
Sedov, L.I.: 1977, *Similarity Methods and Dimensional Analysis in Mechanics*, 8th edn. Moscow Izdatel Nauka. ADS.
Uralov, A.M., Grechnev, V.V., Hudson, H.S.: 2005, Initial localization and kinematic characteristics of the structural components of a coronal mass ejection. *J. Geophys. Res. Space Phys.* **110**, A05104. DOI. ADS.
White, S.M., Loukitcheva, M., Solanki, S.K.: 2006, High-resolution millimeter-interferometer observations of the solar chromosphere. *Astron. Astrophys.* **456**, 697. DOI. ADS.
Yashiro, S., Gopalswamy, N., Michalek, G., St. Cyr, O.C., Plunkett, S.P., Rich, N.B., Howard, R.A.: 2004, A catalog of white light coronal mass ejections observed by the SOHO spacecraft. *J. Geophys. Res. Space Phys.* **109**, A07105. DOI. ADS.
Zandanov, V.G., Lesovoi, S.V.: 1999, Radio observations of filaments at the SSRT. In: Bastian, T.S., Gopalswamy, N., Shibasaki, K. (eds.) *Proc. Nobeyama Symp.*, 37. ADS.
Zheleznyakov, V.V.: 1970, *Radio Emission of the Sun and Planets*, Pergamon Press, Oxford. ADS.
Zheleznyakov, V.V.: 1996, *Radiation in Astrophysical Plasmas*, *Astrophysics and Space Science Library* **204**, Springer, Dordrecht. DOI. ADS.